DOI: 10.1002/chem.200903258

PAMAM Dendrimers for siRNA Delivery: Computational and Experimental Insights

Giovanni Maria Pavan,[a] Paola Posocco,*[b] Aaron Tagliabue,[c] Marek Maly,[a, d] Anastasia Malek,[e] Andrea Danani,[a] Enzio Ragg,[c] Carlo V. Catapano,[e] and Sabrina Pricl[b]

Abstract: Short double-stranded RNAs, which are known as short interfering RNA (siRNA), can be used to specifically down-regulate the expression of the targeted gene in a process known as RNA interference (RNAi). However, the success of gene silencing applications based on the use of synthetic siRNA critically depends on efficient intracellular delivery. Polycationic branched macromolecules such as poly(amidoamine) (PAMAM) dendrimers show a strong binding affinity for RNA molecules and, hence, can provide an effective, reproducible, and relatively nontoxic method for transferring siRNAs into animal cells. Notwithstanding these perspectives, relatively few attempts have been made so far along these lines to study in detail the molecular mechanisms underlying the complexation process between PAMAMs and siRNAs. In this work we combine molecular simulation and experimental approaches to study the molecular requirements of the interaction of RNA-based therapeutics and PAMAM dendrimers of different generations. The dendrimers and their siRNA complexes were structurally characterized, and the free energy of binding between each dendrimer and a model siRNA was quantified by using the well-known MM/PBSA approach. DOSY NMR experiments confirmed the structural *in silico* prediction and yielded further information on both the complex structure and stoichiometry at low N/P ratio values. siRNA/PAMAM complex formation was monitored at different N/P ratios using gel retardation assays, and a simple model was proposed, which related the amount of siRNA complexed to the entropy variation upon complex formation obtained from the computer simulations.

Keywords: binding process · molecular simulations · NMR spectroscopy · PAMAM dendrimers · siRNA delivery

Introduction

The discovery of antisense oligonucleotides (AS-ODNs) and, more recently, small interfering RNAs (siRNAs) has opened wide perspectives in therapeutics for the treatment of cancer, infectious, and anti-inflammatory diseases. However, these molecules are unstable in biological fluids, concomitantly displaying poor intracellular penetration. Nanotechnology can offer a solution to turn these genetic materials into drugs, by allowing the design of new means to overcome most of the barriers that hampered the development of AS-ODN and siRNA therapeutics. These barriers can be summarized as follows: i) protein and enzyme interactions with the carrier or its content, and ii) tissular, cellular, and subcellular targeting.

siRNAs were discovered by showing that the introduction of a long double-stranded RNA (dsRNA) into a variety of hosts could induce post-transcriptional silencing of all homologous host genes and/or transgenes.[1–4] Within the intra-

[a] Dr. G. M. Pavan, Dr. M. Maly, Prof. A. Danani
Physical and Mathematical Sciences Research Unit (SMF)
University for Applied Sciences of Southern Switzerland (SUPSI)
Centro Galleria 2, 6928 Manno (Switzerland)

[b] Dr. P. Posocco, Prof. S. Pricl
Molecular Simulation Engineering (MOSE) Laboratory, DICAMP
University of Trieste, Piazzale Europa 1, 34127 Trieste (Italy)
Fax: (+39) 040-569823
E-mail: posocco@dicamp.units.it

[c] Dr. A. Tagliabue, Prof. E. Ragg
Dipartimento di Scienze Molecolari Agroalimentari (DISMA)
University of Milan, via Celoria 2, 20133 Milano (Italy)

[d] Dr. M. Maly
Department of Physics, J. E. Purkinje University
Ceske mladeze 8, 400 96 Usti nad Labem (Czech Republic)

[e] Dr. A. Malek, Dr. C. V. Catapano
Laboratory of Experimental Oncology
Oncology Institute of Southern Switzerland (IOSI)
Via Vela 6, Bellinzona, 6500 (Switzerland)

Supporting information for this article is available on the WWW under http://dx.doi.org/10.1002/chem.200903258.

cellular compartment, the long dsRNA molecules are metabolized to small 21–23-nucleotide-interfering RNAs by the action of an endogenous ribonuclease: the dsRNA-specific RNAse III enzyme Dicer.[2,5,6] The siRNA molecules then assemble to a multiprotein complex, termed RNA-induced silencing complex (RISC). Functional RISC contains four different subunits, including helicase, exonuclease, endonuclease, and homology-searching domains. When siRNA binds to RISC, the duplex siRNA is unwound by helicase, resulting in two single strands,[7] allowing the antisense strand to bind to the targeted RNA molecule.[3] The endonuclease hydrolyzes the target messenger RNA (mRNA) homologous at the site where the antisense strand is bound. RNA interference has an antisense mechanism of action, as ultimately a single-strand RNA binds to the target RNA molecule by Watson–Crick base pairing rules and recruits a ribonuclease that degrades the target RNA.[8] When siRNA-mediated silencing occurs, the products are cleaved, released, and degraded, allowing the RISC complex to interact with other molecules from the mRNA pool.

siRNAs are natural phosphodiester compounds. However, critical drawbacks such as their poor stability versus nuclease activity both in vitro and in vivo, their low intracellular penetration, and their scarce bioavailability have limited their use in therapeutics.[9,10] All possible barriers and needs for delivery of siRNA to cells have been nicely summarized by Li and Szoka in a recent paper,[11] in which these authors also clarified the needs for suitable vectors to deliver therapeutic genetic material, together with the definition of different approaches for circumventing these hurdles. At first, a delivery system given by the intravenous administration should avoid both interactions with plasma proteins and uptake by the macrophages of the monocyte phagocytic system (MPS). This is really a critical issue, as such interactions result in the formation of aggregates that are trapped in the lung endothelial capillary bed and then taken up by the MPS.[12] Moreover, biocompatibility issues could arise such as complement activation.[13] Similar to classical colloidal drug carriers, delivery systems for nucleic acids should cross the permeable endothelium, such as in neovascularized tumors or inflammation. In such an instance, size effects come into play, as only relatively small particles will be able to pass through the fenestrated capillaries and reach the tumor core or the inflammation site without escaping again into the main stream (enhanced permeability and retention effect, or EPR). Also, before reaching the cellular level, a suitable vectors system should be able to cross the tight network made by the extracellular matrix, composed of a variety of polysaccharides and proteins populating the cell surface.[11] Finally, upon targeting its final destination, the vector still has to face the problems of intracellular penetration, subcellular localization, endosomal escape, and, last but not least, safe and efficient cargo release. The completion and optimization of all these steps need to be part of the rationale to develop new and effective siRNA delivery systems.

Initially, for the purpose of serving as nucleic acid carriers, viral vectors were employed that had the advantage of high transfection efficiency. This characteristic could be traced to the inherent ability of viruses to transport genetic material into the cell as a part of their natural replication and survival pathway. On the other hand, viral systems showed limited loading capacity and, most importantly, posed severe safety risks due to their oncogenic potential, inflammatory, and immunogenic effect, which prevent them from repeated administration. In the light of these problems, concerns, and limitations, nonviral systems have emerged as a promising alternative for gene delivery. As outlined above, the main requirements for these vectors are the protection of their nucleic acid load as well as their efficient uptake into the target cells and subsequent release of the cargo in the cell cytoplasm (or, in the case of DNA, in the cell nucleus). Several delivery strategies were thus developed, which can, however, be classified into two main categories, namely *lipofection* and *polyfection*, the former relying on cationic lipids, whilst the latter is based on the employment of polymers, dendrimers, and peptides.[14] However, unlike viral analogues that have evolved means to overcome cellular barriers and immune defense mechanisms, nonviral gene carriers consistently exhibit significantly reduced transfection efficiency as they still suffer some hindrance from several extra- and intracellular obstacles. At the same time, biocompatibility and potential for large-scale production make these compound classes increasingly attractive for gene therapy.

Owing to the ease of synthesis and commercial availability, polyamidoamine (PAMAM) dendrimers have become one of the most utilized dendrimer-based vectors for gene transfer.[15] The synthesis of these compounds proceeds by a repetitive sequence involving Michael addition of a nucleophilic core (ethylenediamine (EDTA) or ammonia) to methyl acrylate followed by an amidation of the resulting ester with an amine functionality (e.g., EDTA). Starburst PAMAM dendrimers are nanoscopic polymers with a molecular architecture characterized by regular dendritic branching and radial symmetry. The topological structure of these polymers is achieved by the ordered assembly of polymer subunits in concentric, dendritic tiers surrounding an initiator core. The exclusive physical and chemical properties of dendrimers are attributable to the outgrowth of their shape as well as to the high positive charge density, due to the presence of both primary amine groups on the surface of the molecules and tertiary amine moieties within the dendrimer inner branches, which are protonated at physiological (7.4) and lower pH (5) values, respectively.

The unique chemical architecture of PAMAM dendrimers, coupled with their limited size, has stimulated different research groups to explore their applications in biology and medicine, which began by evaluating their toxicity and immunogenicity. Unfortunately, PAMAMs were found endowed with a notable cytotoxicity,[16] substantially related to the formation of cavities in the cell membrane, indicating membrane rupture. This damage was attributed to the cationic nature of PAMAM-NH_2 and appeared to be directly related

to the generation number, concentration, and incubation time with the cells.[17] At the same time, however, these free amine surface groups are essential for enhancing the cytoplasmic delivery of therapeutic molecules.[18] Specifically, the internalization and accumulation of PAMAM-NH_2 dendrimers in the cellular endosomes result in the acidification of the overall environment. As a consequence, protonation of the tertiary amine nitrogen atoms of the dendrimers takes place as a buffering mechanism, which triggers the diffusion and accumulation of Cl^- counterions into the endosomes. These, in turn, result in an increased endosomal osmotic pressure and eventually rupture of the endosomal membrane and release of its contents, including the loaded dendrimers, into the cytoplasm of the targeted cells.[19]

Notwithstanding these problematic issues, PAMAM dendrimers are still considered ideal model systems for understanding the process of uptake and delivery of therapeutic agents including siRNAs, because of their high aqueous solubility, large number of chemically versatile surface groups, and, as said, unique architectures and properties. Under these perspectives, we decided to undertake a coupled experimental/theoretical investigation of classical PAMAM dendrimers and their complexation with a small-interfering RNA. For this purpose, atomistic molecular simulations were performed for dendrimer molecules from generation 1 to generation 6 in the presence of explicit water molecules, counterions, and added ionic strength and at two different values of pH of physiological relevance (7.4 and 5). The most important structural features of these molecules, such as radius of gyration values, fractal dimensions, solvent-accessible surface areas, and radial distribution functions, were thoroughly analyzed and compared with experimental data, where available. The complexes between dendrimer generations most relevant to siRNA delivery applications (i.e., G4 to G6) and a standard reference siRNA sequence (GL3, see the Supporting Information) were then simulated by using a well-validated computational methodology, and the relevant free energy of binding values ΔG_{bind} were estimated.

To complement information stemming from simulations, ^{1}H NMR DOSY spectra were recorded to determine the diffusion coefficients of G4 and G5 PAMAMs and their complexes with siRNA. Also, the values of the hydrodynamic radii for these species (as well as those for the isolated dendrimers) resulting from NMR were compared to those estimated by modeling. Finally, gel retardation assay-based techniques were applied to estimate the binding of G4–G6 and the siRNA at different dendrimer/siRNA charge ratios (N/P), and a two-parameter model for the prediction of these curves, based upon both experimental and theoretical data, was formulated.

Results and Discussion

Dendrimers provide unique dual characteristics of ultrasoft colloids and structural polymers, making them candidates for a variety of biomedical applications ranging from drug delivery to MRI imaging and gene therapy. The pH dependence of the size and structure of the dendrimers is a critical issue for their utilization as drug delivery vehicles in physiologic environments (pH 5 to 7.4). To provide insights into the structure and the properties of dendrimers as a function of generation at various pH conditions, we estimated their radius of gyration R_g and calculated the corresponding radial distribution functions by using fully atomistic MD simulations in explicit solvent, counterions, and ionic strength. Figure 1 shows equilibrated snapshots taken from the MD trajectories of PAMAMs of generation G6 as an example.

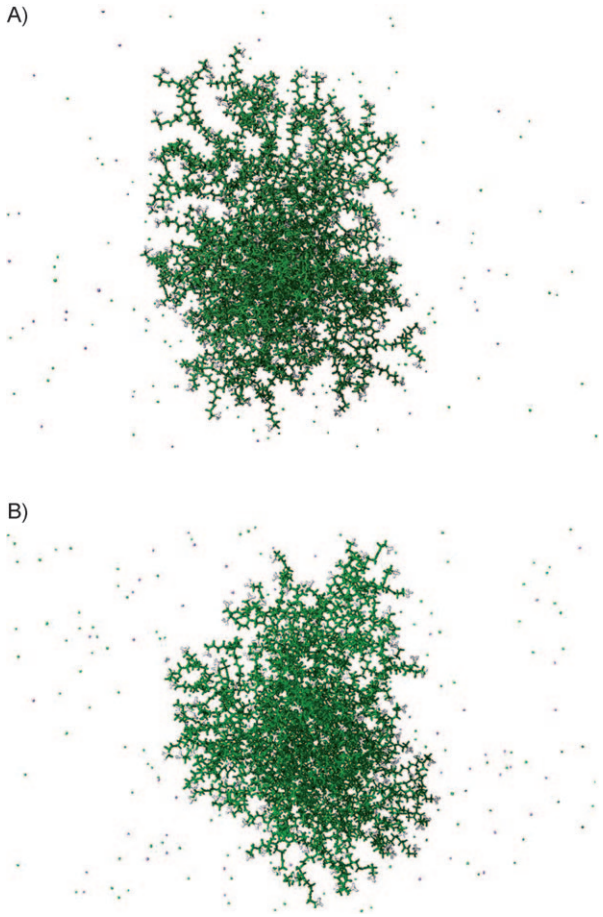

Figure 1. Snapshots taken from MD simulations of PAMAM generation 6 at different protonation levels. A) The low pH (=5) structure, B) the neutral pH (=7.4) structure. Dendrimers are depicted in colored sticks representation, with the terminal NH_3^+ groups highlighted as white ball-and-stick models. Sodium and chlorine counterions are portrayed as purple and green spheres, respectively. Water is omitted from the picture for clarity.

The radius of gyration R_g is a fundamental tool for the description of structural properties of dendrimers. This quantity, related to the square root of the second invariant of the first-order tensor $\boldsymbol{S}$, takes into account the spatial distribution of the atom chain by mediating over all N molecular

components. For a dendrimer, the mean-square radius of gyration is defined by Equation (1),

$$\left\langle R_g^2 \right\rangle = \frac{1}{M_w} \left\langle \left[\sum_{i=1}^{N} m_i |r_i - R|^2 \right] \right\rangle \quad (1)$$

where R is the center of mass of the dendrimer, r_i and m_i are the position and mass of the ith atom, and M_w refers to the total mass of the dendrimer. The R_g values estimated by MD simulations for all generations at different protonation levels (i.e., pH 7.4 and 5) are reported in Figure 2 as a function of the dendrimer molecular weight M_w. Importantly, these values are in excellent agreement with those previously determined by SAXS experiments,[21,22] and with other MD simulations,[23] as evidenced in Table 1.

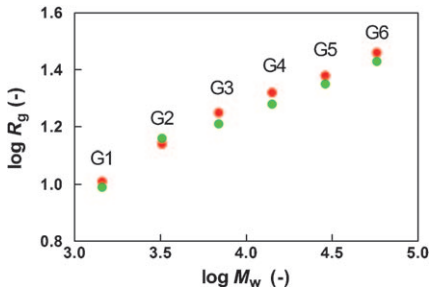

Figure 2. Log–log plot of R_g calculated from MD simulations as a function of the PAMAM molecular weight. Green symbols: pH 7.4; red symbols: pH 5.

As shown in Figure 2 and Table 1, and as expected, the dimensions of the PAMAMs increase with increasing generation and, coherently, the R_g values at lower pH are greater than the corresponding values at pH 7.4 by virtue of the protonation of the tertiary amine nitrogen atoms which, in turn, leads to a molecular expansion by internal charge repulsion. This allows an enhanced water and counterions penetration into the dendrimer branches, with the ultimate consequence of nanovector swelling. This behavior is commonly known as the proton sponge effect,[20] as the influx of water and chlorine counterions to compensate the increased protonation state of the dendrimer makes the nanocarriers behave like a virtual proton sponge.

One of the important problems in supramolecular chemistry is the origin of the specificity and recognition in molecular interaction. An essential step in this process is the complementary contact between approaching molecular surfaces. Surface representation of macromolecules such as, in our specific case, nucleic acids or dendrimers, have provided a powerful approach to characterizing the structure, folding, interactions, and properties of such molecules.[24] A fundamental feature of surfaces that has not been characterized by these representations, however, is the texture (or roughness) of the polymer surface, and its role in molecular interactions has not been defined. Another important, related issue, deals with a basic property of surfaces: their accessibility to incoming molecules depends on their size. Generally, there are three main factors that determine the accessibility of a given ligand to its receptor molecule. The first is the umbrella effect of the ligand, as most molecules have cross-sectional areas that shield more than the molecular locus in which they bind. The second factor is the surface irregularity, tortuosity, and connectivity, and the degree to which these surface features shield the binding points from an incoming molecule. The third parameter is surface heterogeneity, from the point of view of both the possible clustering of binding sites and the difference in affinity of the interacting groups due to inductive effects of the surroundings moieties.

It has been long known in surface science that apparent surface areas decrease with an increase in ligand size, due to the parallel decrease in geometric accessibility. It was found that, in many instances, the relation between these two parameters is given by Equation (2),

$$m \propto \sigma^{-D_f/2} \quad (2)$$

where m is the monolayer value of the bound ligands of cross-sectional area σ, and D_f is often interpreted as the fractal dimension of the surface available to binding. Since it is found that, usually, $2 \leq D_f < 3$, it seems that the simplest interpretation of D_f is that it reflects mainly the geometrical nature of the surface, that is, from a flat surface ($D_f = 2$) up to extreme volume-like irregularity ($D_f = 3$). Equation (2) may be applied, in principle, for the evaluation of the surface roughness and surface accessibility of macromolecules, such as proteins and dendrimers. The degree of geometrical irregularity of a dendrimer is one of the parameters that determine the diffusion kinetics of a small substrate on the surface of the macromolecule or into it. The method of determining the

Table 1. Radius of gyration R_g values [Å] for PAMAM dendrimers obtained from MD simulations at two different pH values (standard deviation in parentheses). For comparison, experimental values obtained through SAXS experiments and theoretical values derived from previous MD simulations are given.

Generation	pH 5	pH 7.4	SAXS[a]			Other MD simulations[b]
G1	10.19 (0.34)	9.85 (0.30)				
G2	13.88 (0.37)	14.44 (0.41)				
G3	17.96 (0.17)	16.25 (0.38)	15.8[c]	16.5[d]	15.09[d]	
G4	21.00 (0.22)	19.00 (0.21)	17.1	17.6	18.6	16.78[e]
G5	24.23 (0.18)	22.43 (0.29)	24.1	25.3	23.07	20.67
G6	28.90 (010)	27.21 (0.11)	26.3	27.5	27.5	26.76

[a] See references [21,22]. [b] See reference [23]. [c] In CH_3OH from sphere model. [d] In CH_3OH from Guinier plot. [e] In explicit water and counterions.

D_f value of dendrimers[24] has been to apply Equation (2) by "covering" the surface of the dendrimers with a monolayer of model spherical molecules of cross-sectional area σ. The area A thus determined is given by Equation (3).

$$A \propto \sigma^{(2-D_f)/2} \tag{3}$$

Table 2 lists the calculated surface fractal dimensions for PAMAM generations G4–G6 at pH 5 and 7.4, as these are the physiological environments at which binding and cell internalization occur, respectively, and G4–G6 are the most relevant generations for biological applications.

Table 2. Surface fractal dimension D_f for PAMAM G4–G6 at pH 5 and 7.4.

Generation	pH 5 D_f	pH 7.4 D_f
G4	2.05	2.02
G5	2.14	2.08
G6	2.18	2.13

It is worthwhile noting that the calculated fractal dimensions for all dendrimer generations at both pHs are quite close to those characterizing various protein and biomacromolecules, which vary, just to cite a few, between 2.05 for DNA to 2.18 for retinol binding protein.[25] The results of this analysis are of much value, especially in the molecular design of pharmaceutical and/or biocompatible molecules, as well as in surface molecular recognition based on similar fractal dimensions, as it seems to be the case between siRNA and PAMAMs.

Another molecular issue, derived from the collected data, is the so-called molecular solvent-accessible surface area (SASA). As SASA clarifies the specificity and recognition in molecular interaction, we again limited the calculation of this property only to dendrimer generations potentially involved in binding. During the MD simulations, a significant solvent penetration to the interior of the dendrimer molecules has been detected, as testified by the corresponding radial distribution functions discussed later in this paper. This water take-up leads to more open molecular structures for the dendrimers. The interaction of the dendrimers with these solvent molecules is largely determined by its SASA.[24a] The SASA is obtained by "rolling" a sphere of radius r_p around the van der Waals surface of the molecule, where r_p represents the effective radius of the solvent (e.g., $r_p = 1.4$ Å for a water molecule). The SASA is then composed of the locus of the probe-sphere midpoints. In principle, the SASA of an ideal, spherical molecule containing no internal voids can be defined by Equation (4),

$$\mathrm{SASA} = 4\pi(R + r_p)^2 \tag{4}$$

in which R and r_p are the radius of the spherical molecule and of the probe, respectively. Accordingly, a plot of $(\mathrm{SASA})^{1/2}$ versus r_p for such an ideal molecule would be linear, with a slope of $2\pi^{0.5}$ and an intercept proportional to the radius R. Typically, real molecules are never exactly spherical, nor free from internal voids. Therefore, for large values of r_p, the SASA is expected to reveal first-order dependence from r_p, whereas, for small values of the probe radius, a deviation from linearity associated with the internal region can be predicted. As can be seen in Figure 3A and B,

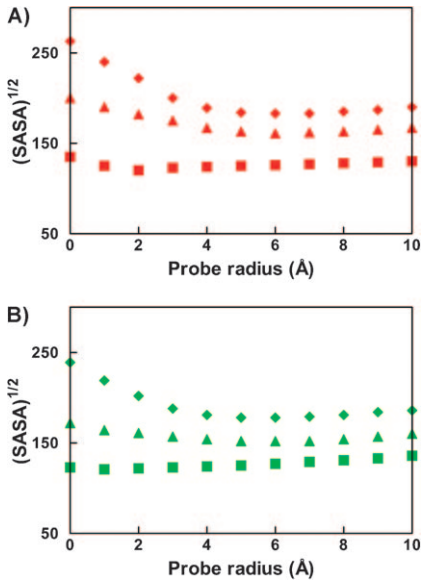

Figure 3. Square root of the solvent-accessible surface area (SASA) as a function of the probe radius for PAMAM generations G4, G5, and G6 at pH 5 (A) and pH 7.4 (B). Symbols: squares: G4; triangles: G5; diamonds: G6.

for large values of r_p, the SASA indeed becomes linear with r_p for both pH values, as expected; nevertheless, for small probe radii, a positive deviation from linearity is observed, owing to the extra surface area associated with the interior regions of the molecules.

For probe radii $r_p > 6$ Å, $(\mathrm{SASA})^{1/2}$ values are proportional to probe radius, indicating that only the exterior surface of the dendrimer is sampled, and suggesting that molecules with a radius $r_p > 6$ Å would not fit inside the dendrimer. As we shall discuss later, this constitutes a direct validation of the MD results relative to the dendriplexes simulations, where the siRNA is mainly bound to the outmost dendrimeric branches and only a few base pairs can penetrate into the inner dendrimer structure for binding. The deviation in SASA at smaller probe radii measures the internal cavities within the dendrimer, and the available internal surface area in a solvent-filled dendrimer. The behavior of $(\mathrm{SASA})^{1/2}$ is qualitatively similar for all PAMAM generations, but the available internal surface area increases with the increase of protonation level, in definite harmony with all evidences discussed above.

As mentioned earlier, parameters such as branch size, shape, and multiplicity can have dramatic effects on the ultimate shape, the interior topology and the exterior surface properties (alias congestion) of the developing molecule. Mathematically, we can appraise dendrimer surface as a function of generation from the relationship given in Equation (5),

$$A_z = \frac{A}{N_z} \propto \frac{R^2}{N_c N_b^G} \tag{5}$$

in which A_z is the surface area per terminal group Z, A is the dendrimer surface area, and N_z is the number for terminal group Z per generation.[15] From this relation we can see that, at higher generations G, A_z becomes increasingly smaller and experimentally approaches the cross-sectional area of the van del Waals dimension of the surface group Z. The generation G thus reached is referred to as the starburst dense-packed (limited) generation. As predicted by de Gennes and Hervet,[26] ideal starburst growth without branch defects is possible only for those generations preceding the dense-packed state. This critical dendrimer property gives rise to self-limiting starburst dimensions, which are a function of the branch-juncture multiplicity N_b and sterical dimensions of the terminal group Z. Since the dendrimer radius R in the expression above is dependent on the dendrimer branch length L_b, larger values of L_b will delay this congestion, whereas larger N_c and N_b values and larger Z dimensions will dramatically hasten it. As shown in Table 3,

Table 3. Surface area per terminal group versus generation for PAMAM G4–G6 at pH 5 and 7.4.

	A_z					
	G1	G2	G3	G4	G5	G6
pH 5	199	226	238	242	241	230
pH 7.4	203	226	234	235	232	233

A_z increases from generation 1 to 4 at all protonation levels, and starts decreasing from generation 5. Accordingly, this analysis allows us to conclude that for this type of dendrimers, the starburst limited generation, that is the generation at which the molecule should exhibit i) sterically inhibited reaction rates, ii) sterically induced stoichiometry, and, quite possibly, iii) a critical phase change due to surface cooperativity, is presumably located in correspondence with G4 at both neutral and acidic pH.

It was previously discussed how, in the presence of a polar solvent like water, a substantial penetration of water inside the macromolecule is observed, which causes the structure to swell as a consequence of the favorable interaction of the solvent with the protonated amines. Moreover, depending of the degree of protonation, a significant fraction of the counterions condense with the dendrimer, residing very close to the protonated sites. As the protonation level increases, there are more counterions inside the dendrimer, and the dendrimer swelling is more pronounced. Figure 4A and B plot the radial density distributions of all PAMAM generations at low and neutral pH, respectively. It can be inferred that, in presence of solvent and both at neutral or low pH, for G1–G6 the density distribution is characterized by a maximum at small R values, and then decreases somewhat monotonically with increasing R. This effect becomes more evident as the pH decreases, and constitutes an indication that the dendrimer core region is denser than the outer part. Because of this hollowness at the middle regions of the molecule, a significant number of water molecules are allowed to penetrate within the dendrimer inner branches.

Another dramatic feature is the high degree of back-folding. The usual schematic diagrams found in the literature for dendrimers, particularly the 2D representations, convey the idea that the terminal groups are located at the periphery of the molecule. However, the actual MD simulations reveal the presence of a substantial back-folding of the end groups toward the dendrimer core. These findings agree with the solid-state NMR measurements on flexible dendrimers,[27] which reveal close contact between the core and peripheral group, and with other atomistic simulations on various dendrimer systems.[28,29] To quantify this aspect, the radial distribution functions for terminal nitrogens for various generations are reported in Figure 4 C and D. This indicates that the end groups are sufficiently flexible to interpenetrate nearly the whole molecule. In particular, the end groups of higher generations come even close to the core of the molecule, and the extent of back-folding increases with the increase of generation. This effect is again more evident at neutral pH; higher generations show evident peaks near the core of the molecule and, for lower generations, the back-folding pervades the entire molecular architecture.

To gain structural and energetic insights, at a molecular level, into the complexation between clinically important PAMAM generations (G4–G6) and siRNA, another set of atomistic MD simulations was performed on the relevant complexes, assuming a simplified stoichiometry of 1 dendrimer:1 siRNA in each respective dendriplex. Figure 5 shows equilibrated snapshots extracted from the corresponding MD trajectories of the G6/siRNA complexes at pH 5 and 7.4, respectively.

To characterize the conformational change of dendrimer and siRNA upon binding, we calculate the values of the radius of gyration of the entire complex, R_g^{compl}, and those of the dendrimer and siRNA within the complex, R_g^{dend} and R_g^{siRNA}, respectively. The values obtained from our MD calculations are reported in Table 4. At both pH values and for each dendrimer generation, R_g^{siRNA} is significantly smaller than R_g^{dend}, testifying the tendency of siRNA to partially penetrate inside the dendrimeric structure. Nevertheless, as expected, the biggest part of the siRNA double helix still remains outside the dendrimer, and this reflects in the R_g^{compl} value being larger than R_g^{dend}. Furthermore, the siRNA is a duplex, and the base pairing/stacking interactions between the opposite strands concur to confer an intrinsic rigidity to

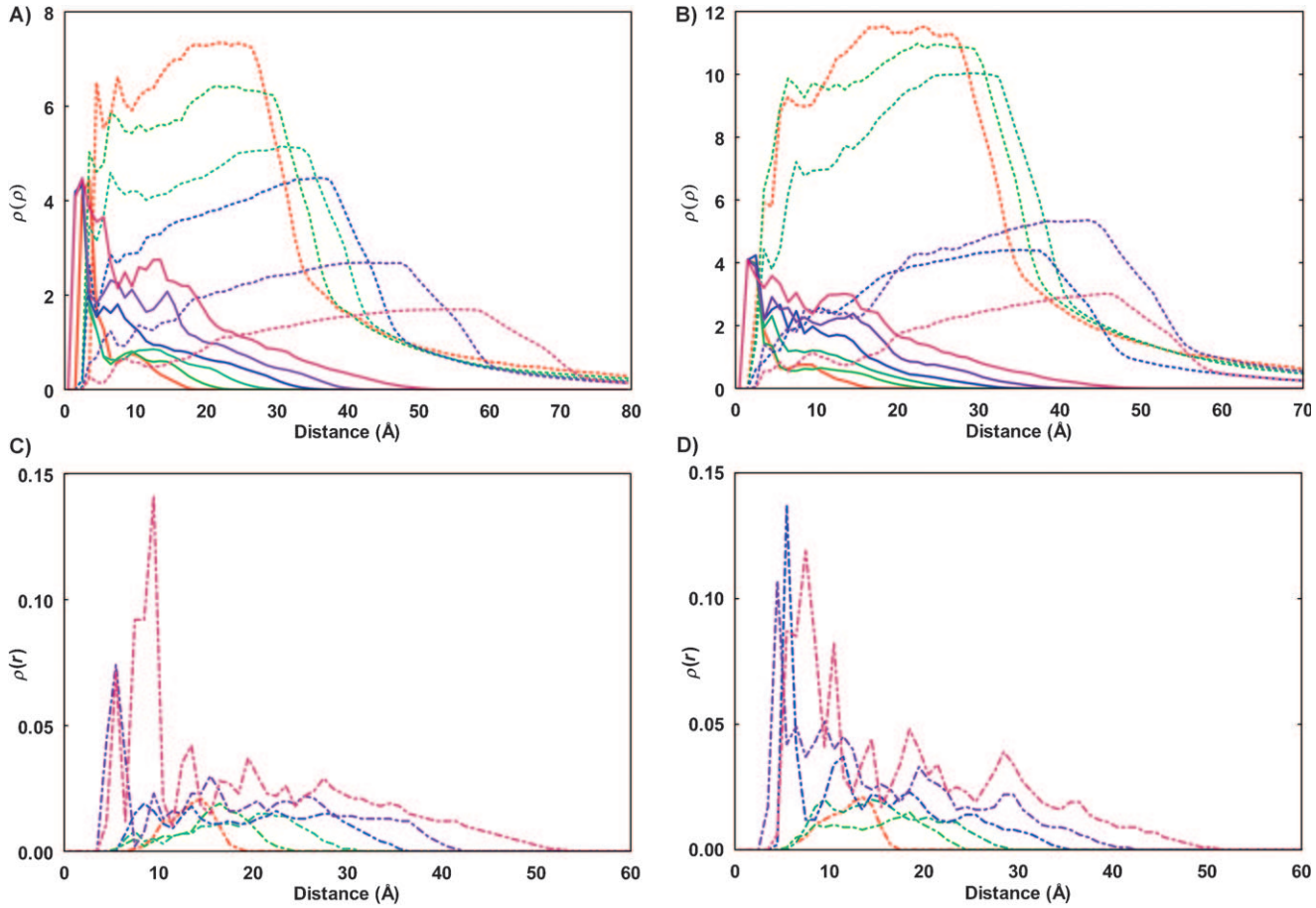

Figure 4. Radial density distributions for PAMAM generations G1 to G6 (continuous lines) and water (broken lines) at pH 5 (A) and pH 7.4 (B). Radial density distributions for terminal nitrogens of PAMAM generations G1 to G6 at pH 5 (C) and pH 7.4 (D). Color code: red: G1; light green: G2; dark green: G3; blue: G4; purple: G5; dark red: G6.

the overall structure, preventing a substantial wrapping of the nucleic acid around the dendrimer surface.

These considerations are also supported by the analysis of the solvent-accessible surface area SASA (vide supra) and of the radial distribution functions reported below in Figure 6.

Comparing Figure 6A and B, it can be seen that, due to the swelling of the polymer, considerable water can penetrate inside the dendrimer. The water uptake seems to be dependent on the dendrimer generation; in particular, at neutral pH, water diffusion within the dendrimer branches decreases as G increases. In any case, water molecules are detected even close to the dendrimer cores at both pH 5 and pH 7.4. Upon siRNA complexation, all PAMAM generations do not appear to undergo major conformational changes, maintaining the dense core configuration observed for isolated dendrimers (see Figure 4A and B). Finally, siRNA density distributions are found well inside the corresponding dendrimer density profiles, indicating that the nucleic acid can easily penetrate into the outmost dendrimer branches, some base pairs reaching deeper into the nanovectors structure.

The free energy of binding values ΔG_{bind} between PAMAMs from generation G4 to generation G6 and the GL3 siRNA sequence were estimated by using the molecular mechanics/Poisson–Boltzmann surface area (MM/PBSA) methodology.[30] These values are reported in Table 5, together with all the energy components contributing to ΔG_{bind}.

As expected for the interaction of two highly, oppositely charged macroions, the electrostatic part of the nonbonded mechanical energy components of ΔG_{bind}, namely ΔE_{ele}, affords the predominant contribution to the binding for each dendrimer generation and at both pH values. On the other hand, due to the polar character of both the nanovectors and cargo, the desolvation penalty paid by these molecules upon binding (ΔG_{PB}) is also quite substantial (see Figure 7A). The corresponding mean values of the van der Waals and hydrophobic overall interaction energies ($\Delta E_{vdW} + \Delta G_{NP}$, see Table 5) contribute approximately to 10% of the overall electrostatic components ($\Delta E_{ele} + \Delta G_{PB}$), thus confirming the substantial electrostatic nature of the interactions in the dendriplexes.

Finally, the calculated changes in solute entropy, $-T\Delta S$, make an unfavorable contribution to the complex formation

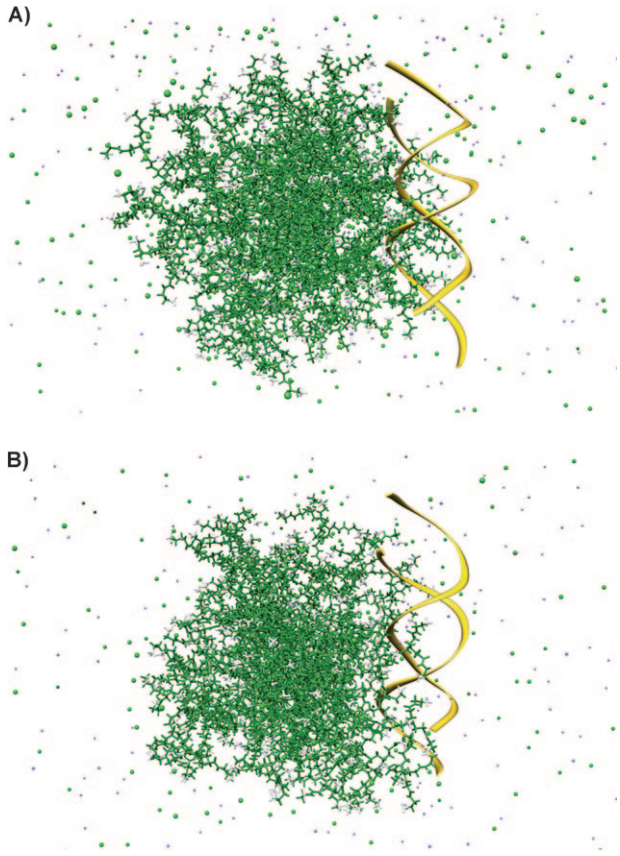

Figure 5. Snapshots taken from MD simulations of PAMAM generations G6 in complex with GL3 siRNA at different protonation levels. Top: low pH (=5) structure; bottom: neutral pH (=7.4) structure. Dendrimers are depicted as colored sticks, with the terminal NH_3^+ groups highlighted as white ball-and-stick models. The siRNA is outlined as a golden ribbon. Sodium and chlorine counterions are portrayed as purple and green spheres, respectively. Water is omitted for clarity.

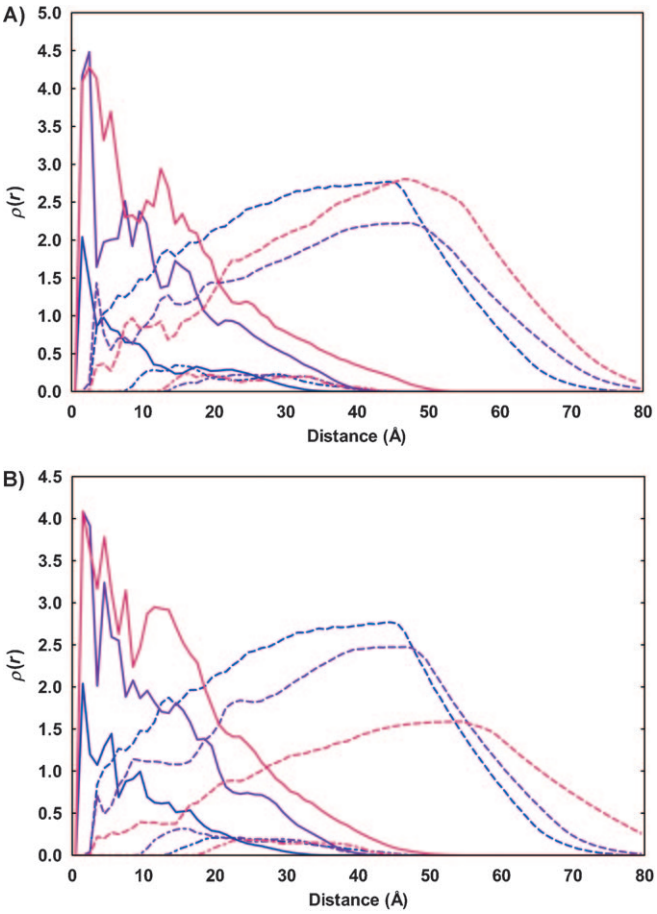

Figure 6. Radial density distributions for PAMAM generations G4 to G6 in complexes with siRNA (continuous lines), water (broken lines), and siRNA (dotted-broken line) at pH 5 (A) and pH 7.4 (B). Color code: blue: G4; purple: G5; dark red: G6.

Table 4. Radius of gyration values R_g^{compl}(Å) for G4–G6 PAMAM dendrimers in complexes with GL3 siRNa (standard deviations in parenthesis). The values for the dendrimer and siRNA within the corresponding complexes, R_g^{dend} and R_g^{siRNA}, are also given.

	pH 5			pH 7.4		
Generation	R_g^{compl}	R_g^{dend}	R_g^{siRNA}	R_g^{compl}	R_g^{dend}	R_g^{siRNA}
G4	23.65	22.06	19.56	23.01	19.56	20.08
	(0.15)	(0.15)	(0.39)	(0.21)	(0.24)	(0.36)
G5	25.83	24.76	18.79	24.81	23.47	20.41
	(0.10)	(0.10)	(0.33)	(0.14)	(0.15)	(0.21)
G6	30.01	29.38	19.76	28.39	27.41	19.43
	(0.14)	(0.08)	(0.35)	(0.07)	(0.08)	(0.33)

in all cases, which increases as the dendrimer generations increase independently of the pH value considered (Figure 7B). A plot of the values of ΔH versus $-T\Delta S$ (taken from Table 5) is shown in Figure 8A. A least-squares linear regression fit of the points (correlation coefficient $R^2=0.98$) demonstrates the linear relationship between the enthalpies and the entropies of siRNA binding to the PAMAMs. As this plot indicates, the binding entropy decreases when the binding enthalpy increases. One explanation for this observation is that as the dendrimer forms favorable interactions by wrapping the siRNA with some of its outer branches, both the dendritic arms and the nucleobases involved in these interactions lose degrees of freedom upon binding. Moreover, solvent molecules and stabilizing counterions associated with the hydration shell of the nanovector and those residing in the binding pocket in the major groove of the siRNA also become rearranged. Similarly, a plot of ΔH versus ΔG_{bind} (shown in Figure 8B) is also linear ($R^2=0.99$), again characteristic of classical enthalpy/entropy compensation.

Enthalpy/entropy compensation is a phenomenon widely observed in biology, and commonly reported for the binding of ligand to proteins, particularly in papers dealing with computational aspects, such as this.[31] In these cases, molecular rationales of the enthalpy/entropy compensation have relied both on the "local freezing" of the molecular parts directly involved in binding, as well as on the involvement of water molecules and mobile ions rearranged in the binding processes. Ordered waters and ions around charged macromolecules clearly are expected to have an important effect upon binding; accordingly, when a siRNA duplex binds to

Table 5. Free energy of binding and its component for the formation between PAMAM G4, G5, and G6 and GL3 siRNA under two pH conditions of physiological interest, as obtained from MM/PBSA calculations. All values are in kcal mol^{-1}. Standard errors of the means are reported in parentheses.

	pH 7.4			pH 5.0		
	G4/GL3	G5/GL3	G6/GL3	G4/GL3	G5/GL3	G6/GL3
ΔE_{vdW}	−44.58	−66.50	−71.29	−87.18	−114.57	−135.77
	(5.93)	(9.70)	(9.18)	(9.49)	(13.18)	(15.22)
ΔE_{ele}	−27186.60	−51796.44	−86827.58	−57630	−100315.04	−158934.28
	(210.40)	(364.56)	(1493.61)	(619.27)	(678.29)	(2382.03)
ΔE_{MM}	−27231.18	−51862.94	−86898.88	−57717.68	−100429.61	−159070.05
	(209.94)	(364.32)	(1500.45)	(624.39)	(689.07)	(2398.29)
ΔG_{NP}	−11.12	−17.56	−15.21	−20.14	−24.46	−26.33
	(0.57)	(1.39)	(1.78)	(1.97)	(1.94)	(1.91)
ΔG_{PB}	26870.38	51227.80	85901.50	56985.10	99307.69	157252.06
	(203.46)	(354.70)	(1480.93)	(603.46)	(682.91)	(2292.85)
ΔH	−371.92	−652.69	−1012.59	−752.72	−1146.38	−1844.32
	(13.71)	(13.85)	(29.70)	(27.97)	(35.81)	(31.78)
$-T\Delta S$	+64.78	+101.64	+228.79	+154.47	+284.42	+577.06
	(3.64)	(13.14)	(25.64)	(16.74)	(29.23)	(56.88)
ΔG_{bind}	−307.14	−551.05	−783.80	−598.25	−861.96	−1267.26

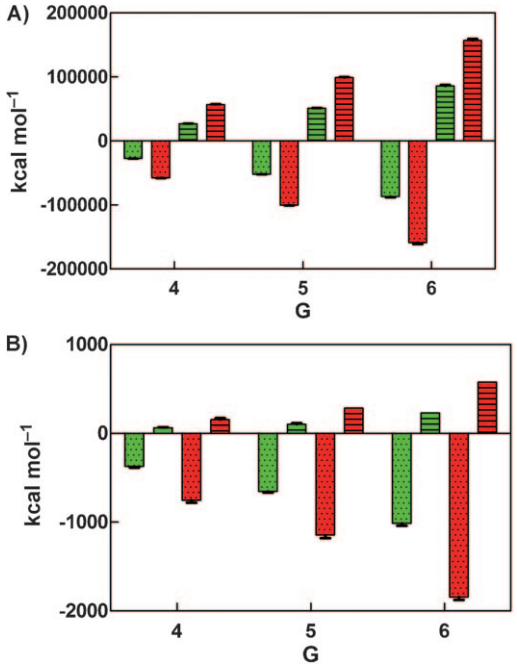

Figure 7. A) Comparison of the electrostatic ΔE_{ele} and polar solvation ΔG_{PB} contributions to the binding free energy of GL3 siRNA to PAMAM G4–G6 at two different pH values: 7.5 (green bars) and 5 (red bars). Dotted bars: ΔE_{ele}; horizontally lined bars: ΔG_{PB}. B) Comparison of the enthalpic ΔH and entropic $-T\Delta S$ contributions to the binding free energy of GL3 siRNA to PAMAM G4–G6 at two different pH values: 7.5 (green bars) and 5 (red bars). Dotted bars: ΔH; horizontally lined bars: $-T\Delta S$. (see Table 5 and Supporting Information for more details).

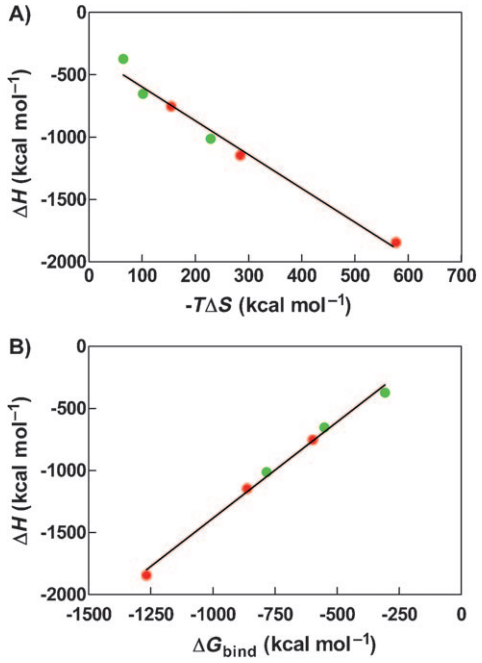

Figure 8. Relationship between the enthalpy and the entropy of siRNA binding to G4–G6 PAMAM dendrimers at two different pH: 7.5 (green symbols) and 5 (red symbols). A) Plot of ΔH versus $-T\Delta S$ and B) plot of ΔH versus ΔG_{bind}. The two solid lines through the data are the best fit lines (see Table 5 and Supporting Information for more details).

an oppositely charged PAMAM molecule, the base pairs of the nucleic acid involved in the interaction undergo some alteration and become locally distorted to accommodate the dendrimer moieties. This results in a local stretching of the phosphate backbone that alters and reduces some degree of freedom at the binding zone.[32] The latter change also reduces the local charge density and would necessarily result in the release of condensed counterions,[32,33] which partly attenuate the substantial decrease in entropy of the macroions upon binding. Also, many important direct and indirect interactions are expected to take place between the dendrimer, siRNA, and the surrounding solvent; formation of specific hydrogen bonds between the nanovectors and the siRNA can also possibly be mediated by bridging waters. Water layer rearrangements along the major groove at the binding site, coupled with the specific van der Waals and electrostatic interactions discussed above, and a variety of new and reoriented stacking interactions all likely contribute to the formation of the relevant dendriplex.

The foregoing discussion about the radius of gyration highlighted the importance of this parameter in quantifying the molecular size of dendrimers and their siRNA complexes, as well as their molecular behavior in solution. Another quantity, strictly related to R_g, is the hydrodynamic radius R_h. Experimentally, R_h can be estimated by using the Stokes–Einstein equation, which relates the diffusion coeffi-

cient D (as measured e.g., by NMR DOSY experiments) to the hydrodynamic radius of the object undergoing translational motion according to Equation (6),

$$R_h = \frac{RT}{6\pi\eta D} \tag{6}$$

in which k is the Boltzmann constant, T is the temperature (in K), and η is the medium viscosity. R_g and R_h are two closely related, although not identical, quantities, the latter taking into account both the contribution of solvent molecules and shape effects. Figure 9 shows the linear correlation

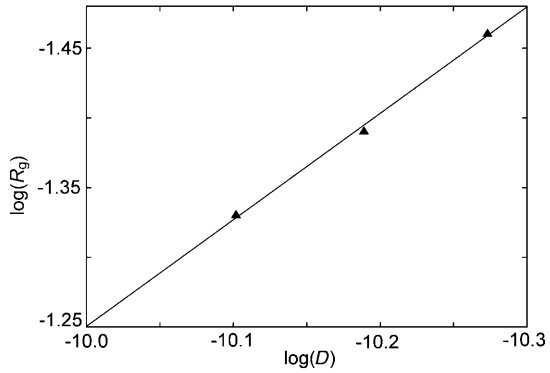

Figure 9. Linear correlation of experimental log(D) versus theoretical log(R_g) values, derived from DOSY experiments and MD calculations, respectively, for G4–G6 dendrimers at neutral pH. [PAMAM] = 31 μM, D_2O, NaCl 0.15 M, T = 298 K. Correlation coefficient (R^2) is 0.99.

between experimental values of log(D) and the theoretical values of log(R_g), derived from NMR DOSY experiments and MD calculations, respectively (see Table 1), for PAMAM G4–G6 at acidic, neutral, and basic pH values.

From the experimental standpoint, the pure GL3 siRNA and the dendrimer solutions (G4 and G5) were also studied by using ^{1}H NMR spectroscopy (see Figure 10). The spectrum recorded for GL3 shows, in the region between δ = 3.5 and 6 ppm, resonances attributable to ribose and pyrimidine 5-H protons, whereas the low-field peaks in the δ = 6–8 ppm region are due to pyrimidine 6-H, and purine 8-H or 2-H protons.[34]

Addition of PAMAM to the GL3 solution caused an extensive line-broadening of both RNA and dendrimer NMR resonances, due to the increase in the molecular correlation time as a result of complex formation. This made rather difficult a reliable measurement of diffusion coefficients, based on the observation of the RNA signals. However, the δ = 2.7–3.55 ppm region of the NMR spectrum is characterized by resonances arising only from the PAMAM side chains and is devoid of any RNA resonance (see trace A and B in Figure 10). This region was found suitable for the measurement of diffusion coefficients based on dendrimer signals alone, as any interference from the GL3 resonance is prevented in the numerical analysis. In this region, the sharp triplets attributable to the methylene groups of the external

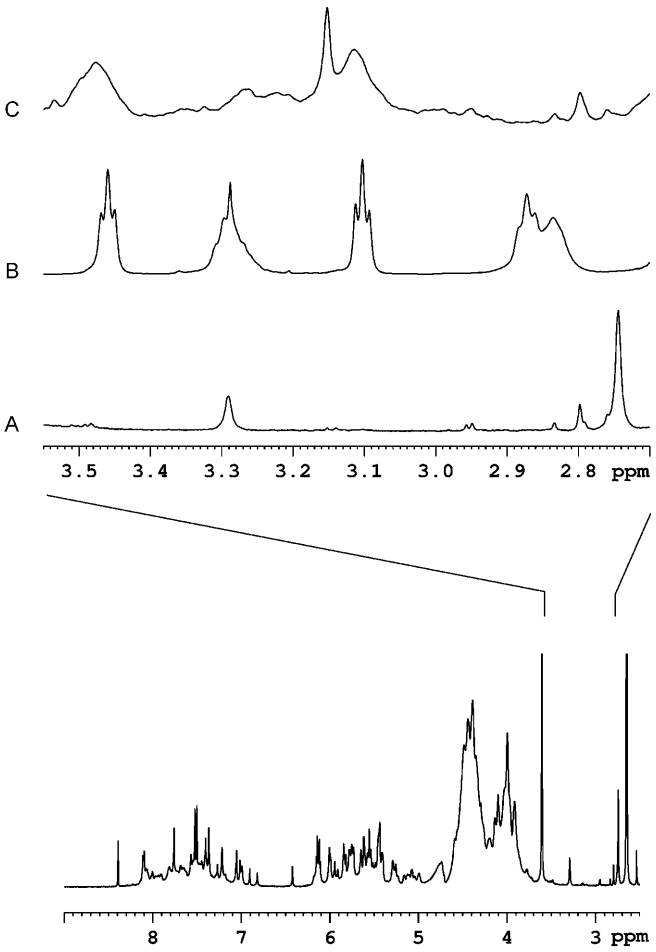

Figure 10. ^{1}H NMR spectrum (600 MHz) of a 75 μM GL3 siRNA solution. Trace A: expansion of the δ = 2.7–3.55 ppm region of the same spectrum; trace B: expansion of a ^{1}H NMR spectrum of dendrimer G5; trace C: expansion of a ^{1}H NMR spectrum of a siRNA/G5 mixture at a molar ratio [siRNA]/[G5] = 21. Solution conditions: D_2O 100%, NaCl 0.15 M, phosphate buffer 20 mM, pH 7.0.

side chains are evident at δ = 3.46 (-CONHCH_2CH$_2$NH$_3^+$) and 3.1 ppm (-CONHCH$_2$$CH_2NH_3^+$), together with the methylene groups located in the α-position with respect to the tertiary amines at δ = 2.8 ppm (-NH$^+$$CH_2CH_2$CONH-) and to the inner amides at δ = 3.3 ppm (-CONHCH_2CH$_2$NH$^+$-)

The last trace in Figure 10 (trace C) illustrates the ^{1}H NMR spectrum of the GL3 siRNA/G5 PAMAM complex. The spectrum shows a substantial modification in the δ = 2.7–3.5 ppm region, where the dendrimer signals experienced both a chemical shift and a line-width variation. The triplets, originating from the external CH_2 groups, were the least affected, as they are characterized by an intrinsic major amplitude of the segmental motions, with respect to the inner groups.

Pseudo two-dimensional DOSY experiments were thus carried out using a gradient-based stimulated echo bipolar pulse sequence.[35] DOSY yields a two-dimensional map that correlates NMR chemical shifts with the corresponding mo-

lecular self-diffusion coefficients *D*. The chemical shifts are employed for resonance assignments (see discussion above), whereas the self-diffusion coefficients *D* can be used to estimate the average molecular weights and the hydrodynamic radii R_h of the molecular systems under investigation. Accordingly, a linear correlation of log(*D*) values versus log(M_w) was derived by using several standards, as depicted in Figure 11, from which the M_w values of PAMAM G4–G6 and those of the dendriplexes siRNA/G4 and siRNA/G5 could be derived on the basis of the experimentally determined *D* values.

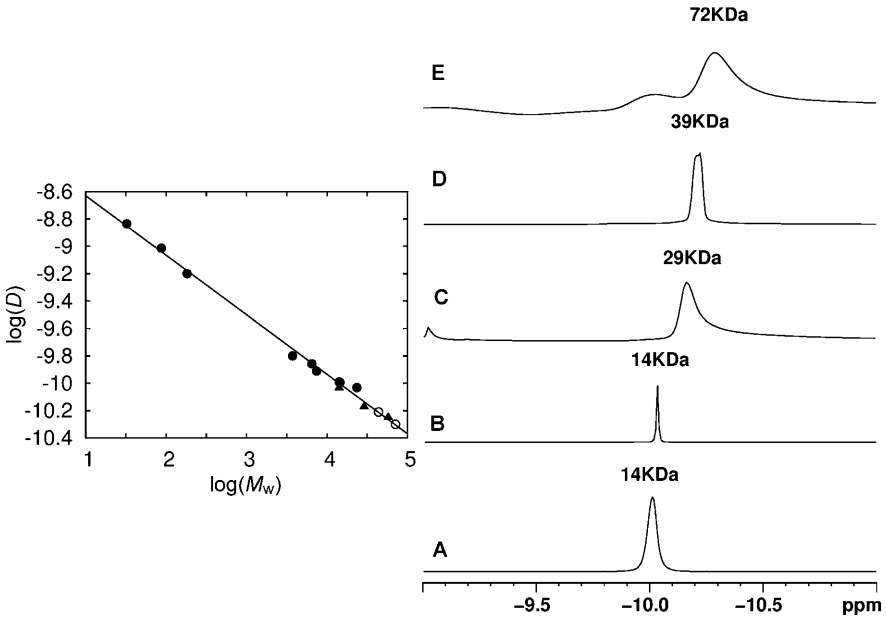

Figure 11. Left: Linear correlation of diffusion coefficients, log(*D*), measured by DOSY experiments, versus molecular weight, log(M_w). The derived equation is: $\log(D) = -0.433\log(M_w) - 8.1987$, correlation coefficient (R^2) is 0.99. The following data are displayed: molecular weight standards (●); log(*D*) of PAMAM G4–G6, measured at pH 8 (▲); predicted log(M_w) values for siRNA/G4 and siRNA/G5 complexes (○). Note that GL3 siRNA was also included as an additional standard (see Supporting Information for details). Right: Projections of the pseudo-2D DOSY experiments for the estimation of M_w values for PAMAM G4 (trace A), siRNA (trace B), PAMAM G5 (trace C), siRNA/G4 dendriplex (trace D), and siRNA/G5 dendriplex (trace E).

As expected, the three M_w values for the pure dendrimers and the nucleic acid are in excellent agreement with the calculated ones (see the Supporting Information for more details). More important, however, are the data relevant to the dendriplexes. Indeed, under the conditions in which the actual DOSY experiments were carried out, the estimated molecular weight for the PAMAM G4/siRNA complex is around 39 kDa, suggesting a stoichiometry of 1 G4:2 siRNA molecules for this dendriplex. On the other hand, in the case of G5 the corresponding molecular weight of the dendriplex is approximately 72 kDa, resulting in a complex stoichiometry of 1 G5:3 siRNAs. These results can be rationalized on the basis of both dendrimer surface charges and dimensions. In fact, G4 being smaller and characterized by less protonated amines on its surface, is able to bind a lower number of nucleic acid charges than the larger and more surface-charged G5 counterpart.

The ability of the different PAMAM generations to form dendriplexes with GL3 siRNA was further investigated by using gel retardation-based assays. The application of a quantitative procedure[36] for the analysis of dendriplexes formation between G4, G5, and G6 with siRNA led to the interesting results illustrated in Figure 12. Indeed, the siRNA/PAMAM complexation curves are characterized by the same sigmoidal shape, irrespective of the dendrimer generation. Interestingly, similar sigmoidal trends were obtained by using entirely different techniques for studying the aggregation of various types of nucleic acids with PAMAMs by Bielinska et al.,[37] thus providing direct support to the present case. The position of the flex points in all curves locate at approximately the same value of N/P, that is, 4.6, again irrespective of G and in the range reported in the literature for closely related systems.[38] Therefore, according to this experimental evidence, PAMAM generations G4 to G6, currently found endowed with promising delivery capacities as nanovectors, do not seem to show any generation-dependent effect in the in vitro binding of GL3 siRNA in a wide range of N/P ratios.

In the attempt to relate the above information with some parameters stemming from the MM/PBSA analysis of the MD simulations, a simple mathematical relationship was formulated as given in Equation (7),

$$Y(R) = \frac{A}{1 + \exp(\frac{R - R_{50}}{B})} \quad (7)$$

in which the $Y(R)$ is the percentage of complexed siRNA at a given N/P ratio *R*, and *A* is a constant equal to the maximum amount of complexed siRNA (i.e., 100 %). R_{50} is the value for which $Y(R) = 50$, that is the N/P ratio at which 50 % of siRNA complexation by the nanovectors is attained. As discussed above, this parameter is independent of G and, for biologically relevant PAMAM generations (G4–G6), is equal to 4.6. The application of this methodology to siRNA binding by other dendrimer families in the same interval of dendrimer generations (i.e., G4–G7) (data not shown) not only confirmed the general validity of the approach, but

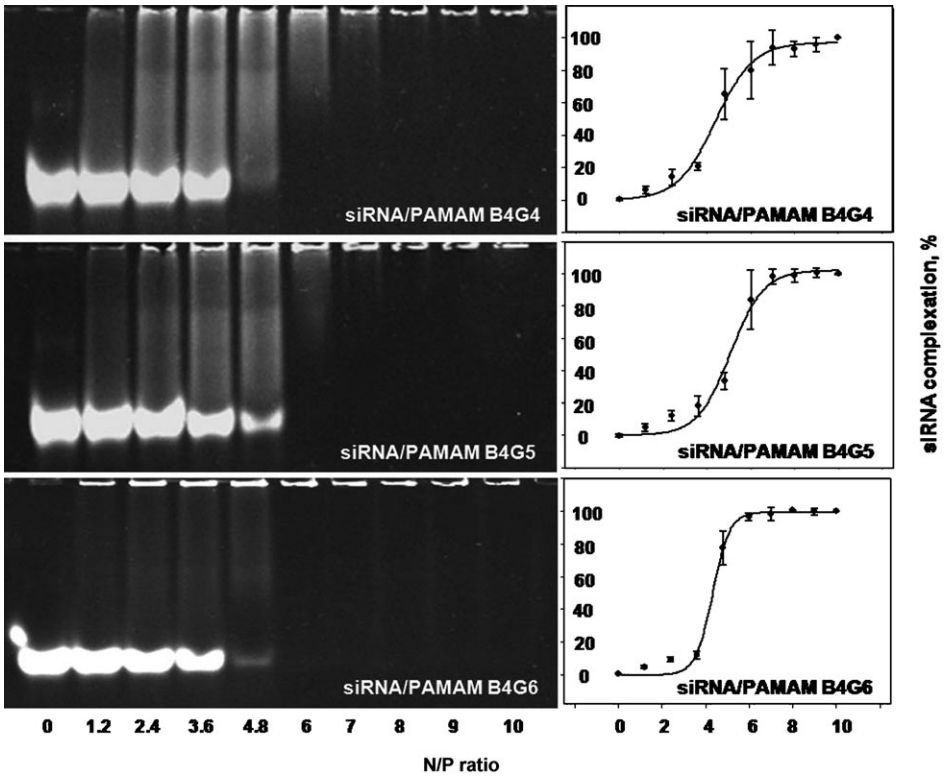

Figure 12. Gel electrophoresis of PAMAM G4/siRNA (A), G5/siRNA (B), and G6/siRNA (C) complexes at varying N/P ratios. Percent of complexed siRNA was evaluated from each assay according to the methods described in Figure 13, and plotted against the N/P ratio for complexation with PAMAM G4 (D), G5 (E), and G6 (F). Each point represents the mean ±standard deviation ($n=3$). Lines are predicted binding curves using the two-parameter models proposed in this work ([Eq. (7)]).

also the fact that R_{50} is uniquely dependent on the dendrimer chemical structure and not on the dendrimer generation number.

Finally, B is a coefficient accounting for the dynamics of complexation and, as such, should, in principle, be dependent on the dendrimer generations. To have a model in which all parameters were non empirical in nature and, as such, linked to molecular features, we checked which component of the free energy of binding, ΔG_{bind}, could eventually be related to B. Interestingly, we found a linear relationship [Eq. (8)] between B and the entropy variation upon binding ($T\Delta S$) values reported in Table 5 (see Figure 13).

$$B = -0.0029 \times -T\Delta S + 1.0483 \quad (8)$$

The results of the binding curves for G4–G6 PAMAMs and GL3 siRNA at different N/P ratios predicted by using Equation (7) and the B value estimated by using Equation (8) are illustrated as continuous lines in Figure 12D, E, and F, respectively. As can be seen from these panels, the agreement between predicted and experimental curves is excellent. Although undisputedly more tests are needed for validation, this model, which depends upon two parameters only (one of which (R_{50}) can be easily determined experimentally and the other (B) can be computed by using the well-known MM/PBSA approach), constitutes a predictive model for the formation of siRNA dendriplexes limiting, in principle, the number of laboratory experiments.

Conclusion

Gene-based therapy has attracted significant attention over the past two decades as a potential method for treating genetic disorders as well as an alternative method to traditional chemotherapy used in treating cancer. In particular, due to its high efficacy and specificity, RNAi has already become the standard method for gene targeting in vitro and is gaining increasing relevance for the therapeutic in vivo breakdown of pathologically relevant genes. Since target gene-specific siRNAs play a pivotal role in triggering RNAi, their efficient delivery is one major challenge both in vitro and in vivo.[39] For several reasons, including cost considerations and biosafety, the non-viral delivery of siRNA is preferred over the alternative viral approaches. Owing to the ease of synthesis and commercial availability, PAMAM dendrimers are among the most utilized dendrimer-based vectors for gene transfer.[40] Notably, it has been shown recently that PAMAMs possess strong binding affinity for RNA molecules,[41,42] interact tightly with group I intron ribozymes,[41] and, last but not least, can efficiently deliver siRNA and thus induce gene silencing in cell cultures.[43]

Notwithstanding these perspectives, relatively few attempts have been made so far along these lines to study in detail the molecular mechanisms underlying the complexa-

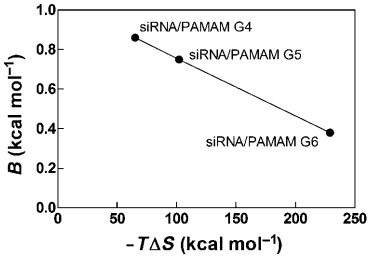

Figure 13. Linear relationship ([Eq. (8)]) between the coefficient B in Equation (7) and the entropy variation upon binding ($-T\Delta S$) values obtained from the estimation of ΔG_{bind} for G4, G5, and G6 PAMAMs and GL3 siRNA using MD simulations in the MM/PBSA framework of theory.

tion process between PAMAMs and siRNAs. We report herein a comprehensive study in which fully atomistic molecular dynamics simulations were coupled to NMR and gel-retardation assays with the purpose of studying the molecular requirements of the interaction of RNA-based therapeutics and PAMAM dendrimers of different generations. The calculated structural parameters for PAMAMs at different pH were in excellent agreement with the actual NMR experiments; also, the fractal dimensions estimated at two biologically important pH values for all dendrimer generations were quite close to those characterizing various protein and biomacromolecules.

By applying the well-validated MM/PBSA computational approach, we then quantified the affinity between a model siRNA and G4–G6 PAMAMs, and the complexes were structurally characterized. Interestingly, both at acidic and neutral pH, and for each dendrimer generation, the MD trajectory revealed the tendency of siRNA to partially penetrate inside the dendrimeric structure. Nevertheless, as expected, the biggest part of the siRNA double helix still remains outside the dendrimer. The values of the ΔG_{bind} components substantiated the electrostatic prevalence in the interactions between the genetic material and the dendrimers, and also revealed the existence of an enthalpy/entropy compensation effect upon binding.

NMR experiments confirmed the structural in silico predictions and yielded further information on both the complex structure and stoichiometry at low N/P ratio values. Indeed, according to the pseudo-2D DOSY experiments, in excess siRNA, PAMAM G4 is able to bind two GL3 molecules, whereas G5, by virtue of both higher charge density and larger dimensions, is able to accommodate three GL3 siRNA onto its surface.

Lastly, based on gel retardation assays, siRNA/PAMAM complex formation at different N/P ratios was monitored, leading to the discovery that the value at which 50% of the siRNA complexation by the nanovectors is attained is independent of the dendrimer generation and, for relevant PAMAM generations (G4–G6), is equal to 4.6. Also, a simple model was proposed that related the amount of siRNA complexed to the entropy variation upon complex formation, as obtained from the computer simulations.[54]

Experimental Section

Computational details: All molecular dynamics (MD) simulations and data analysis were performed with the AMBER 9 suite of programs.[44] Dendrimers were parameterized by using the General Amber Force Field (GAFF),[45] whereas the Amber99 force field[46] was used for parameterization of the GL3 siRNA ligand. At neutral pH (ca. 7.4) all the primary amines were considered to be protonated, whereas at low pH (ca. 5), both primary and tertiary amines were considered protonated. The 21 base-pair double-stranded GL3 siRNA model was generated with the Nucgen module of AMBER 9. Both siRNA and dendrimer molecules were solvated in a TIP3P water box,[47] and a suitable number of Na^+ and Cl^- counterions were added to neutralize the system and to reproduce the ionic concentration of organic solutions. All structures were energy minimized; then, molecular dynamics runs were conducted in three major steps: i) warming, to bring the system to 300 K (100 ps), ii) equilibration (4 ns), and iii) production (4 ns).

From the trajectories of these MDs, representative equilibrated structures of G4–G6 PAMAMs and of GL3 siRNA were extracted and used in the building of the corresponding complexes. The resulting molecular assemblies were solvated, and a suitable number of counterions were added to ensure electrical neutrality. A total of six dendrimer–siRNA complexes were obtained (G4, G5, and G6 with GL3 under two different pH conditions: 7.4 and 5). All energetic analyses were performed for a single MD trajectory of each dendrimer/GL3-siRNA complex, with 100 unbound dendrimer and siRNA snapshots taken from the frames in the equilibrated data production phase of that trajectory.

The binding free energy for each ligand/dendrimer system, ΔG_{bind}, was calculated according to the molecular mechanics/Poisson–Boltzmann surface area method (MM/PBSA)[30] given in Equations (9) and (10).

$$\Delta G_{bind} = \Delta H_{bind} - T\Delta S_{bind} \quad (9)$$

$$\Delta H_{bind} = \Delta E_{gas} + \Delta G_{sol} \quad (10)$$

The average values of the enthalpic contribution to ΔG_{bind} were calculated by summing the gas-phase energies ($\Delta E_{gas} = \Delta E_{ele} + \Delta E_{vdw}$) and the solvation free energies ($\Delta G_{solv} = \Delta G_{PB} + \Delta G_{NP}$).[48] The polar component of ΔG_{solv} was evaluated by using the Poisson–Boltzmann (PB) approach,[49] whilst the nonpolar contribution to the solvation energy was calculated as $\Delta G_{NP} = \gamma$ (SASA) + β, in which $\gamma = 0.00542$ kcal Å^{-2}, $\beta = 0.92$ kcal mol^{-1}, and SASA is the solvent-accessible surface area estimated with the MSMS program.[50] Finally, from the production dynamic simulation, 10 snapshots, from the original 100 were selected and the normal-mode analysis approach was applied to estimate the last parameter: the entropic contributions ($-T\Delta S$).[51]

All simulations of dendrimers, GL3-siRNA molecules, and complexes were conducted on the CINECA BCX IBM BladeCenter LS21 Cluster and on the Tartaglia cluster of the University of Trieste, working in parallel on 32 processors.

NMR experiments: The NMR spectra were recorded at 25 °C on a Bruker AV600 spectrometer operating at a frequency of 600.10 MHz for the ^{1}H nucleus. Chemical shifts (δ) were measured in ppm. ^{1}H NMR spectra were referenced to external 2,2-dimethyl-2-silapentane-5-sulfonate sodium salt (DSS) set at 0.00 ppm. DOSY experiments were performed on a 500 µL solution of siRNA/dendrimer complexes in a [siRNA]/[PAMAM] molar ratio equal to 21. Resonance assignments for PAMAMs were performed by using standard two-dimensional homonuclear shift correlation techniques. Pseudo two-dimensional DOSY experiments were acquired by using a gradient-based stimulated echo bipolar pulse sequence.[35,52]

A linear correlation of $\log(D)$ values versus $\log(M_w)$ was derived by using different standards.[53] The GL3 siRNA was also included as an additional standard. Linear least-squares fitting was achieved by using Equation (11), with a correlation coefficient R^2 of 0.9947.

$$\log(D) = -0.4333 \times \log(M_w) - 8.1987 \quad (11)$$

siRNA/PAMAM complexation assay: To determine the efficiency of the complex formation between siRNA and PAMAM G4-G6 dendrimers, each corresponding mixture of siRNA and PAMAM underwent electrophoresis in the presence of GelRed (1:10000) at 80 mV for 1 h. RNA was visualized under UV light by using the InGenius gel analysis system, and quantified by using the ImageJ software. Since the degree of complexation was reflected both by the amount of shifted RNA and the velocity of shifting, both these parameters were considered. Briefly, the amount of RNA in each gel line was estimated as the maximal volume of signal intensity, whilst the velocity of RNA run was assumed as a shift of the "center of mass of the signal" from the starting point. The product of the two parameters was calculated for each sample, and normalized relative to the two outermost samples: free RNA and completely complexed RNA. Formation of any specific siRNA/PAMAM complex in the appropriate range of N/P ratio was assayed in triplicate; the means of the vol-

umes and standard deviations were fitted to a three-parameter sigmoid function using SigmaPlot software.

The siRNA sequence employed, and the detailed description of all the computational and experimental procedures adopted in this work is available in the Supporting Information.

Acknowledgements

The financial support from the DRUDE Initiative, project "Nanovectors for drug delivery in oncology: a combined modeling/experimental study" performed under the project framework "Computational Life Science-Ticino in Rete" sponsored by DECS-Canton Ticino and USI (A.D., C. V. C., and S.P.) is acknowledged. This research has been carried out under the EU Framework Program COST Action TD0802 "Dendrimers in Biomedical Applications" .

[1] A. Fire, S. Xu, M. K. Montgomery, S. A. Kostas, S. E. Driver, C. C. Mello, *Nature* **1998**, *391*, 806–811.
[2] S. M. Elbashir, J. Harborth, W. Lendeckel, A. Yalcin, K. Weber, T. Tuschl, *Nature* **2001**, *411*, 494–498.
[3] H. Vaucheret, M. Fagard, *Trends Genet.* **2001**, *17*, 29–35.
[4] J. R. Kennerdell, S. Yamaguchi, R. W. Carthew, *Genes Dev.* **2002**, *16*, 2654–2659.
[5] L. Timmons, A. Fire, *Nature* **1998**, *395*, 854.
[6] R. F. Ketting, S. E. Fischer, E. Bernstein, T. Sijen, G. J. Hannon, R. H. Plasterk, *Genes Dev.* **2001**, *15*, 2654–2659.
[7] A. Nykanen, B. Haley, P. D. Zamore, *Cell* **2001**, *107*, 309–321.
[8] P. D. Zamore, T. Tuschl, P. A. Sharp, D. P Bartel, *Cell* **2000**, *101*, 25–33.
[9] J. B. Opalinska, A. M. Gewirtz, *Nat. Rev. Drug Discovery* **2002**, *1*, 503–514.
[10] D. M. Dykxhoorn, J. Lieberman, *Cell* **2006**, *126*, 231–235.
[11] W. Li, F. C. Szoka, *Pharm. Res.* **2007**, *24*, 438–449.
[12] P. Opanasopit, M. Nishikawa, M. Hashida, *Crit. Rev. Ther. Drug Carrier Syst.* **2002**, *19*, 191–233.
[13] C. Planck, K. Mechtler, F. C. Szoka, E. Wagner, *Gene Ther.* **1996**, *3*, 1437–1446.
[14] M. A. Mintzer, E. E. Simanek, *Chem. Rev.* **2009**, *109*, 259–302.
[15] D. A. Tomalia, A. N. Naylor, W. A. Goddard III, *Angew. Chem.* **1990**, *102*, 119–157; *Angew. Chem. Int. Ed. Engl.* **1990**, *29*, 138–175.
[16] R. Duncan, L. Izzo, *Adv. Drug Delivery Rev.* **2005**, *57*, 2215–2237.
[17] M. El-Sayed, M. Ginski, C. Rhodes, H. Ghandehari, *J. Controlled Release* **2002**, *81*, 355–365.
[18] N. D. Sonawane, F. C. Szoka, A. S. Verkman, *J. Biol. Chem.* **2003**, *278*, 44826–44831.
[19] O. Boussif, F. Lezoualc'h, M. A. Zanta, M. D. Mergny, D. Scherman, B. Demeneix, J.-P. Behr, *Proc. Natl. Acad. Sci. USA* **1995**, *92*, 7297–7301.
[20] J.-P. Behr, *Chimia* **1997**, *51*, 34–36.
[21] T. J. Prosa, B. J. Bauer, E. J. Amis, D. A. Tomalia, R. Scherrenberg, *J. Polym. Sci. Polym. Chem. Ed.* **1997**, *35*, 2913–2924.
[22] S. Rathgeber, M. Monkenbusch, M. Kreitschmann, V. Urban, A. Brulet, *J. Chem. Phys.* **2002**, *117*, 4047–4062.
[23] a) P. K. Maiti, T. Cagin, S. T. Lin, W. A. Goddard III, *Macromolecules* **2005**, *38*, 979–991; b) P. K. Maiti, R. Messina, *Macromolecules* **2008**, *41*, 5002–5006.
[24] a) P. Posocco, M. Ferrone, M. Fermeglia, S. Pricl, *Macromolecules* **2007**, *40*, 2257–2266; b) L. Metullio, M. Ferrone, A. Coslanich, S. Fuchs, M. Fermeglia, M. S. Paneni, S. Pricl, *Biomacromolecules* **2004**, *5*, 1371–1378; c) S. Pricl, M. Fermeglia, M. Ferrone, A. Asquini, *Carbon* **2003**, *41*, 2269–2283; d) M. Fermeglia, M. Ferrone, S. Pricl, *Bioorg. Med. Chem.* **2002**, *10*, 2471–2478; e) S. Pricl, M. Fermeglia, *Carbohydr. Polym.* **2001**, *45*, 23–33; f) E. Blasizza, M. Fermeglia, S. Pricl, *Mol. Simul.* **2000**, *24*, 167–189.
[25] K. S. Birdi. *Fractals in Chemistry, Geochemistry and Biophysics*, Plenum, New York, **1993**.
[26] P. G. de Gennes, H. J. Hervet, *J. Phys. Lett.* **1983**, *44*, 351–360.
[27] K. L. Wooley, C. A. Klug, K. Tasaki, J. Schaefer, *J. Am. Chem. Soc.* **1997**, *119*, 53–58.
[28] C. B. Gorman, M. W. Hager, B. L. Parkhurst, J. C. Smith, *Macromolecules* **1998**, *31*, 815–822.
[29] C. B. Gorman, J. C. Smith, *Polymer* **2000**, *41*, 675–683.
[30] J. Srinivasan, T. E. Cheatham, P. Cieplak, P. A. Kollman, D. A. Case, *J. Am. Chem. Soc.* **1998**, *120*, 9401–9409.
[31] For a selection papers dealing with this topic from our group see, among others: a) G. M. Pavan, A. Danani, S. Pricl, *J. Am. Chem. Soc.* **2009**, *131*, 9686–9694; b) D. Zampieri, M. G. Mamolo, E. Laurini, M. Fermeglia, P. Posocco, S. Pricl, E. Banfi, G. Scialino, L. Vio, *Bioorg. Med. Chem.* **2009**, *17*, 4693–4707; c) M. Tonelli, I. Vazzana, B. Tasso, V. Boido, F. Sparatore, M. Fermeglia, M. S. Paneni, P. Posocco, S. Pricl, P. La Colla, C. Ibba, B. Secci, G. Collu. R. Loddo, *Bioorg. Med. Chem.* **2009**, *17*, 4425–4440; d) M. Mazzei, E. Nieddu, M. Mielea, A. Balbia, M. Ferrone, M. Fermeglia, M. T. Mazzei, S. Pricl, P. La Colla, Marongiu, C. Ibba, R. Loddo, *Bioorg. Med. Chem.* **2008**, *16*, 2591–2605; e) D. Zampieri, M. G. Mamolo, L. Vio, E. Banfi, G. Scialino, M. Fermeglia, M. Ferrone, S. Pricl, *Bioorg. Med. Chem.* **2007**, *15*, 7444–7458; f) A. Carta, M. Loriga, G. Paglietti, M. Ferrone, M. Fermeglia, S. Pricl, T. Sanna, C. Ibba, C. P. La Colla, R. Loddo, *Bioorg. Med. Chem.* **2007**, *15*, 1914–1927.
[32] J. B. Chaires, *Biopolymers* **1997**, *44*, 201–215.
[33] C. Bailly, X. Qu, F. Anizon, M. Proudhomme, J. Riou, J. B. Chaires, *Mol. Pharmacol.* **1999**, *55*, 377–385.
[34] K. Wüthrich, *NMR of Proteins and Nucleic Acids*, Wiley, New York, **1986**.
[35] D. Wu, A. Chen, C. S. Johnson, Jr., *J. Magn. Reson. Series A* **1995**, *115*, 260–264.
[36] A. Malek, F. Czubayko, A. Aigner, *J. Drug Targeting* **2008**, *16*, 124–139.
[37] A. U. Bielinska, C. Chen, J. Johnson, J. R. Baker, Jr., *Bioconjugate Chem.* **1999**, *10*, 843–850.
[38] K. Fant, E. K. Esbjörner, P. Lincoln, B. Nordén, *Biochemistry* **2008**, *47*, 1732–1740.
[39] A. Aigner, *Appl. Microbiol. Biotechnol.* **2007**, *76*, 9–21.
[40] R. K. Palanirajan, V. Kumar, N. K. Jain, *Chem. Rev.* **2009**, *109*, 49–87.
[41] J. Y. Wu, J. H. Zhou, F. Q. Qu, P. H. Bao, Y. Zhang, L. Peng, *Chem. Commun.* **2005**, 313–315.
[42] J. H. Zhou, J. Y. Wu, X. X. Liu, F. Q. Qu, M. Xiao, Y. Zhang, L. Charles, C.-C. Zhang, L. Peng, *Org. Biomol. Chem.* **2006**, *4*, 581–586.
[43] J. H. Zhou, J. Y. Wu, N. Hafdi, J.-P. Behr, P. Erbacher, L. Peng, *Chem. Commun.* **2006**, 2362–2364.
[44] D. A. Case, T. A. Darden, T. E. Cheatham, III, C. L. Simmerling, J. Wang, R. E. Duke, R. Luo, K. M. Merz, D. A. Pearlman, M. Crowley, R. C. Walker, W. Zhang, B. Wang, S. Hayik, A. Roitberg, G. Seabra, K. F. Wong, F. Paesani, X. Wu, S. Brozell, V. Tsui, H. Gohlke, L. Yang, C. Tan, J. Mongan, V. Hornack, G. Cui, P. Beroza, D. H. Mathews, C. Schameister, W. S. Ross, P. A Kollman, AMBER 9, University of California, San Francisco, **2006**.
[45] J. Wang, R. M. Wolf, J. W. Caldwell, P. A. Kollman, D. A. Case, *J. Comput. Chem.* **2004**, *25*, 1157–1174.
[46] W. D. Cornell, P. Cieplak, C. I. Bayly, I. R. Gould, K. M. Merz, D. M. Ferguson, D. C. Spellmeyer, T. Fox, J. W. Caldwell, P. A. Kollman, *J. Am. Chem. Soc.* **1995**, *117*, 5179–5197.
[47] W. L. Jorgensen, J. Chandrasekhar, J. D. Madura, R. W. Impey, M. L. Klein, *J. Chem. Phys.* **1983**, *79*, 926–935.
[48] B. Jayaram, D. Sprous, D. L. Beveridge, *J. Phys. Chem. A* **1998**, *102*, 9571–9576.
[49] D. Sitkoff, K. A. Sharp, B. Honig, *J. Phys. Chem.* **1994**, *98*, 1978–1988.
[50] M. F. Sanner, A. J. Olson, J. C. Spehner, *Biopolymers* **1996**, *38*, 305–320.
[51] I. Andricioaei, M. J. Karplus, *J. Chem. Phys.* **2001**, *115*, 6289–6292.

[52] G. Wider, V. Dotsch, K. Wüthrich, *J. Magn. Reson. Ser. A* **1994**, *108A*, 255–258.
[53] L. Scaglioni, S. Mazzini, R. Mondelli, S. Dallavalle, S. Gattinoni, S. Tinelli, G. L. Beretta, F. Zunino, E. Ragg, *Bioorg. Med. Chem.* **2009**, *17*, 484–491.
[54] NOTE ADDED IN PROOF (24.2.2010): During the production process another related paper appeared (G. M. Pavan, L. Albertazzi, A. Danani, *J. Phys. Chem. B* **2010**, *114*, 2667–2675) presenting data in agreement with the findings reported herein.

Received: November 28, 2009
Published online: May 21, 2010

